Journal of Materials Research and Technology 34 (2025) 2512–2526

Contents lists available at ScienceDirect

Journal of Materials Research and Technology

journal homepage: www.elsevier.com/locate/jmrt

Enhanced biomechanical and biological performance of titanium scaffolds with gradient in pore sizes

Ara Jung [a,b,1], Jinju Jang [c,d,1], Hun Yeong Ban [c,e], Hee Jin Kim [a,b], Bomi Gweon [a,**], Dohyung Lim [a,c,*]

[a] Department of Mechanical Engineering, Sejong University, Seoul 05006, Republic of Korea
[b] Department of Biomedicine & Health Sciences, The Catholic University of Korea, Seoul 06591, Republic of Korea
[c] Corporate Research Institute, RNX Inc., Bucheon 14558, Republic of Korea
[d] Department of Mechanical Engineering, Yonsei University, Seoul 03722, Republic of Korea
[e] Department of Medical Engineering, Yonsei University College of Medicine, Seoul 03722, Republic of Korea

ARTICLE INFO

Keywords:
Powder bed fusion
3D metal printing
Osteointegration
Osteogenesis
Neovascularization

ABSTRACT

With the rapid advancement of metal 3D printing technologies, porous metal implants are increasingly explored for regenerative medicine. Among various methods, powder bed fusion (PBF) stands out for its precision in implant design and fabrication. This study systematically investigates the structural, mechanical, and biological aspects of titanium scaffolds using PBF technology with varying pore sizes (400 μm, 600 μm, 800 μm, and 1000 μm). Micro-CT cross-sectional images revealed slight deviations in pore size and structure thickness from the intended designs, yet the overall structure adhered closely to specifications. Mechanical testing showed that as pore size increased, both the elastic modulus and yield strength decreased, with scaffolds in the 600–1000 μm range resembling the properties of human cortical bone. Osteoblast proliferation and differentiation were most active in scaffolds with 1000 μm pores, whereas endothelial cell proliferation thrived in 400 μm pores. To simultaneously enhance mechanical properties, osteointegration, and vascularization, scaffolds with a gradient in pore sizes from 400 μm to 1000 μm were designed and evaluated. These graded scaffolds demonstrated mechanical properties comparable to human cortical bone. In vitro experiments further supported the advantages of pore-size gradients, revealing accelerated osteoblast and endothelial proliferation in the Type 2 gradient scaffolds, featuring a gradient from the center (1000 μm) to the periphery (400 μm). Collectively, these findings suggest that the design strategy of the Type 2 gradient scaffold is beneficial not only for achieving biomechanical compatibility by closely mimicking natural bone but also for promoting osteogenesis and neovascularization.

1. Introduction

Orthopedic implants play a crucial role in treating bone defects, fractures, and joint degeneration, which further provide essential mechanical support to restore skeletal function and enhance patient mobility [1]. Recent research in orthopedic implants has focused on enhancing their biomechanical properties and biocompatibility, as well as improving fixation through biological integration, to achieve better clinical outcomes [2–7].

Traditional orthopedic procedures, including the use of bone cement for fixation, have shown favorable clinical outcomes. However, there are reports that persistent shear and tensile forces that can compromise initial fixation, leading to loosening of implant components [8,9]. The generation of particulate debris at the implant interface also raises concerns about potential local inflammation [10]. Furthermore, studies have indicated that implant can cause stress shielding at the bone-implant interface due to a significant discrepancy in mechanical properties between the implant and the surrounding bone [9,11–13]. As implants bear a significant portion of the load-bearing function, adjacent bone experiences reduced mechanical stress. Prolonged exposure of the bone to this stress shielding effect can lead to bone resorption and weakening over time, compromising the overall stability of the

* Corresponding author. Department of Mechanical Engineering, Sejong University, Seoul 05006, Republic of Korea.
** Corresponding author.
E-mail addresses: bgweon@sejong.ac.kr (B. Gweon), dli349@sejong.ac.kr (D. Lim).
[1] Equal contribution.

https://doi.org/10.1016/j.jmrt.2024.12.216
Received 2 September 2024; Received in revised form 11 December 2024; Accepted 24 December 2024
Available online 24 December 2024

bone-implant interface and the long-term success of the implant [11,12]. The significance of these challenges is underscored by the increasing global life expectancy, which contributes to a rising prevalence of orthopedic cases and joint failures, including late implant failures in the context of extended life spans.

To address these challenges, recent advancements in metal additive manufacturing (AM), notably powder bed fusion (PBF) technology, have emerged as a crucial avenue for improving biocompatibility and fixation [14]. PBF technology is promising due to its ease of implant design and exceptional fabrication precision. The growing demand for porous implants has rendered PBF technology even more noteworthy, as these porous implants can bring significant benefits by enabling customization of their mechanical properties to match those of the surrounding bone tissue, effectively mitigating the stress shielding issue [15–20]. Moreover, porous implants play a key role in promoting bio-integration by facilitating bone ingrowth into the implant structure, thereby providing a practical solution to challenges associated with traditional fixation methods [21,22].

Numerous studies have explored optimal pore design concerning size and shape to provide a conducive environment for bone tissue formation within porous structures [7,23–27]. These investigations have focused on both the mechanical properties and the biological outcomes resulting from pore design. Multiple investigations have examined mechanical properties across various pore designs, consistently reporting that an increase in porosity or pore size generally leads to a decrease in elastic modulus of the implants [16,24,28]. Although the elastic modulus of the porous implants is influenced by factors such as pore shape, density, distribution, and structural thickness, it generally was shown to align closely with that of natural bone tissue, facilitating biomechanical compatibility [15,29,30]. In terms of biological performance, studies on osteogenic functions concerning pore designs have also been reported. For instance, Huri et al. highlighted the significance of scaffold pore size, particularly around the range of 1 mm, in influencing human adipose-derived stem/stromal cell (ASC) osteogenesis. They demonstrated that ASC cells grown on larger pores (1000–1500 μm) exhibited enhanced osteogenic responses compared to those on smaller pores (500–1000 μm and <500 μm), suggesting the pivotal role of pore size in facilitating osteointegration in engineered bone substitutes [23]. Similarly, another study revealed that porous Ti6Al4V implants fabricated via PBF with approximately 600 μm pore sizes exhibited superior bone ingrowth and implant stability compared to those with smaller (400 μm) or larger (800 μm) pores [24]. In addition, our previous investigation elucidated how pore shapes in Ti6Al4V scaffolds, produced through the PBF method, impact surface topography, subsequently influencing the proliferation and differentiation of human osteoblast-like cell (Saos-2). This finding underscores the crucial role of meticulous pore size and shape design in enhancing bone ingrowth efficiency in orthopedic implants [31]. Collectively, these studies emphasize the importance of optimizing scaffold pore characteristics to achieve enhanced osteointegration.

In addition to optimizing pore characteristics for osteointegration, it is crucial to design pores that can promote neovascularization to facilitate new bone formation because adequate vascularization ensures the supply of nutrients and oxygen to developing tissue [32–35]. Recognizing the importance of neovascularization in tissue regeneration, numerous studies have explored the relationship between scaffold pore size and vascularization efficiency [36–40]. The research by Feng et al. demonstrated the impact of pore size on neovascularization in β-tricalcium phosphate (β-TCP) cylinders implanted in rabbits. They found that pore sizes smaller than 400 μm led to increased fibrous tissue ingrowth and limited neovascularization, whereas sizes around 600–700 μm exhibited better vascularization outcomes [37]. Similarly, Wang et al. investigated the vascularization effects of porous Ti6Al4V scaffolds with varying pore sizes (800, 900, and 1000 μm) printed in a regular and irregular manner. Results demonstrate that scaffolds with irregular large pores (1000 μm) exhibit stronger vascularization capabilities than those with regular smaller (800, and 900 μm) pore structures, particularly evidenced by enhanced expression of angiogenesis-related genes [36]. Conversely, in another study, human umbilical vein endothelial cells (HUVECs) were grown on polymer scaffolds with three different pore sizes (5–20 μm, 20–45 μm, and 45–90 μm), and the cells grown on the smaller pore sizes (5–20 μm) showed the best proliferation characteristics [39]. Additionally, another study explores how pore size influences neovascularization in poly (D, L-lactide-*co*-glycolide) inverse opal scaffolds, finding that small pores (147 μm) facilitate the formation of dense networks of small vessels, while large pores (312 μm) promote the development of sparse networks with larger vessels [40].

Table 1
Parameters of the porous scaffolds.

Structure thickness (μm)	Normal type				Gradient type (1 & 2)	
	200				200	
Pore size (μm)	400	600	800	1000	400-1000 (top-bottom gradient)	400-1000 (center-outside gradient)

In designing an optimal implant, a comprehensive assessment which includes mechanical properties, osteogenic efficacy, and vascularization efficiency is essential. Mechanical properties must be finely tuned to minimize stress shielding, while the efficacy of osteogenic and vascularization process should be enhanced to support bone ingrowth and integration with the bone tissue. Previous reports indicate that the optimal pore size or structure varies depending on the specific characteristic to be optimized. However, there remains a gap in the literature concerning a unified approach that comprehensively addresses all these characteristics. Our study aims to fill this gap by systematically manipulating pore size to develop an ideal pore structure that integrates all critical factors. We examined the mechanical and biological attributes of metal scaffolds fabricated using PBF technology at four different pore sizes—400, 600, 800, and 1000 μm—focusing on their efficacy in promoting the proliferation of osteoblasts and endothelial cells. Additionally, we tested scaffolds with a graded pore sizes ranging from 400 μm to 1000 μm. The results reveal that scaffolds featuring a gradient in pore size, especially those with a gradient from the center to the periphery, provide the best mechanical and biological performance. This design strategy not only achieves biomechanical compatibility by mimicking natural human bones but also promotes osteogenesis and neovascularization. These findings confirm the significant potential of utilizing functionally graded pore sizes to gain improved clinical outcomes.

2. Materials and methods

2.1. Designing porous titanium scaffolds

The porous titanium scaffolds were designed using CAD software (Rhino 6/Grasshopper, Robert McNeel & Associates) and its Grasshopper plugins, employing Voronoi-Tessellation method. Our approach included constructing algorithms for finely controlling the distribution of random points, thereby enabling precise control over the density of Voronoi cells. To design scaffolds with varying pore sizes and to implement gradients in pore sizes, the number of Voronoi cells was controlled through Cubic-Bezier curve. In particular, we designed two types of gradient scaffolds: Type 1, with a pore size gradient from top to bottom, and Type 2, with a pore size gradient from the center to the periphery (Fig. S1). The design parameters are detailed in Table 1 and the processes are described in Fig. S2.

2.2. Fabrication of titanium scaffolds

The titanium scaffolds were made by a PBF machine (Metalsys 150E;

Winforsys Co., Ltd.) (Fig. S3), and Ti–6Al–4V alloy powder (Grade 23 ELI, ASTM F3001, Tekna) was used. Based on the datasheet, the powders are spherical with diameters in the range of 15 μm–45 μm. The 3D-printing parameters were set as follows: laser power at 100 W, scan speed at 950 mm/s, hatching spacing at 0.07 mm, and layer thickness at 0.03 mm. All scaffolds were built at an angle of 45° on the building platform. These scaffolds were used in their as-built state without any additional post-processing. Following fabrication, the specimens were cleaned using a standard protocol outlined in Supplementary Table S1.

2.3. Structure characterization of porous titanium scaffolds

Micro-computed tomography (micro-CT) imaging system (Xradia 620 Versa, Carl Zeiss) was used to analyze the structural characteristics of each porous titanium scaffold. The titanium scaffolds were mounted on a revolving stage within the micro-CT system and scanned. The acquired scan data consisted of 975 cross-sectional images with voxel size of 1.5 μm. The pore size and structure thickness were measured from the obtained cross-sectional images of each sample with different pore sizes. As shown in Fig. S4, the pore size and structure thickness were measured manually using ImageJ software (NIH). To obtain the pore size, we drew a circle to fit within the cross-section of the pore and measured the diameter, and, to obtain the thickness of the structure forming the scaffold, we drew a straight line along the width of the structure and measured the length of the line.

Then, 3D models of the scaffolds were reconstructed from the images using commercial software (Mimics/3-Matic, Materialise). From the reconstructed 3D model, surface area and porosity for each scaffold were determined. The surface area was determined using values provided by the software. To measure porosity, we first measured the volume of a solid cylinder model with 0% porosity (V_{total}) and the volume of the reconstructed scaffold model (V_{recon}). We then determined the volume of the pores by calculating the difference between these two volumes ($V_{pore} = V_{total} - V_{recon}$), and subsequently measured porosity through the ratio of V_{pore} to V_{total} (Fig. S5).

2.4. Scanning electron microscopy (SEM) imaging

Field emission scanning electron microscopy (FE-SEM, SU8700, Hitachi) was used to observe the surface morphology of the porous scaffolds. Before imaging, a thin layer of platinum was deposited on the scaffold surface to prevent electron discharge. Imaging was then performed at an acceleration voltage of 20 kV with magnifications of ×35 and × 130.

2.5. Mechanical properties

Mechanical tests were performed in compliance with ISO13314, an international testing standard for porous metallic structure. For each scaffold design, the mechanical test was repeated six times. As illustrated in Fig. S6, titanium scaffolds for each porous structure were fabricated to a size (φ = 10.4 mm, height = 12.38 mm) that could be mounted on the test machine. A universal testing machine (AG-250kNX, Shimadzu) was used, and compression was applied at a speed of 1 mm/min. The load (N) and stroke (mm) values recorded during the compression test were converted into stress (MPa) and strain (%) values using the equations below to obtain the stress-strain curve.

$$Stress\ (MPa) = \frac{Load\ (N)}{Area\ (mm^2)}, Strain\ (\%) = \frac{Stroke\ (mm)}{Height\ (mm)} \times 100$$

Then, the slope of the linear elastic region in the stress-strain curve was measured to calculate the elastic modulus (E), and the yield strength was determined using the 0.2% offset stress method.

2.6. Cell culture

To study bone ingrowth behavior on these titanium scaffolds, we used Saos-2 cells, and to investigate neovascularization behavior, we utilized human umbilical vein endothelial cells (HUVECs). Saos-2 (#80023, Korean Cell Line Bank) cells were grown and sub-cultured in Minimum Essential Medium Eagle (MEM, #Lm007-01, Welgene) supplemented with 10% fetal bovine serum (FBS, #S001-01, Sigma), and 1% Antibiotic-Antimycotic (Anti-Anti, #CA002-010, GenDEPOT). HUVECs were purchased from Lonza (#C2517A) and cultured in endothelial cell basal medium-2 (EBM-2, #CC-3156, Lonza) with EGM-2 SingleQuots Kit (#CC-4176, Lonza).

2.7. Preparation of titanium scaffolds for in vitro experiment

Prior to conducting the in vitro experiment, porous titanium scaffolds were sonicated with a 1% Solujet (#2101, Alconox) solution at 45 °C twice. Subsequently, the scaffolds were thoroughly rinsed by sonicating in distilled water four times at 45 °C. This entire sonication process with Solujet and water was repeated once more for comprehensive cleaning. Following the washing step, the titanium scaffolds were autoclaved at 120 °C for 20 min and dried in a dry oven at 60 °C.

2.8. Quantification of cell proliferation

To evaluate osteoblast proliferation, porous titanium scaffolds were placed in a 24-well plate (#32024, SPL Life Science) and Saos-2 cells were seeded at a density of 4.8×10^4 cells per well. To evaluate endothelial cell proliferation, HUVECs were seeded on the titanium scaffolds in the same manner as Saos-2 cells.

Then, cell counting kit-8 (CCK-8, #CK04, Dojindo Molecular Technologies) were utilized to quantify the number of cells. Quantification was performed at various time points, specifically at 3, 7, 10, and 14 days of cell cultivation. At each time point, cell culture media were removed from the well containing the titanium scaffolds, and 400 μL of the CCK-8 mixture (10% of the culture media volume) was added to each well, followed by incubation in a CO_2 incubator at 37 °C for 90 min. Subsequently, 100 μL of the CCK-8 assay mixture was transferred from each well and placed in a 96-well plate for optical density measurement. The optical density (OD) at 450 nm was determined with a microplate reader (AMR-100, Allsheng, China). Data.

2.9. Quantification of osteoblast differentiation

For quantifying the differentiation of osteoblasts, we employed an alkaline phosphatase (ALP) assay kit (#ab83369, Abcam). Following 14 days of cultivation, the media were harvested and centrifuged at 13000 rpm at 4 °C for 10 min to remove cell debris. The subsequent steps with the ALP assay kit were performed according to the provided instruction manual. The media was introduced into a 96-well plate, and a 5 mM *p*-Nitrophenyl Phosphate (pNPP) solution was added to induce the reaction. This lysate-pNPP mixture was incubated at 25 °C for 60 min, after which the reaction was stopped by the addition of a stop solution. The OD was then measured at 405 nm using a microplate reader (AMR-100, Allsheng).

2.10. Immunofluorescence imaging

To visualize cell adhesion on the titanium scaffolds, Saos-2 cells were cultured on the scaffolds for 14 days. After culturing, the scaffolds were removed from the well-plate and gently washed with phosphate-buffered saline (PBS). The cells on the porous titanium scaffolds were then fixed with 3.7% formaldehyde solution for 10 min, permeabilized with 0.2% TritonX-100 solution for 10 min, and washed with PBS. Subsequently, the cells were incubated with rhodamine phalloidin (1:50, #R415, Invitrogen) for 1 h and stained with Hoechst 33342

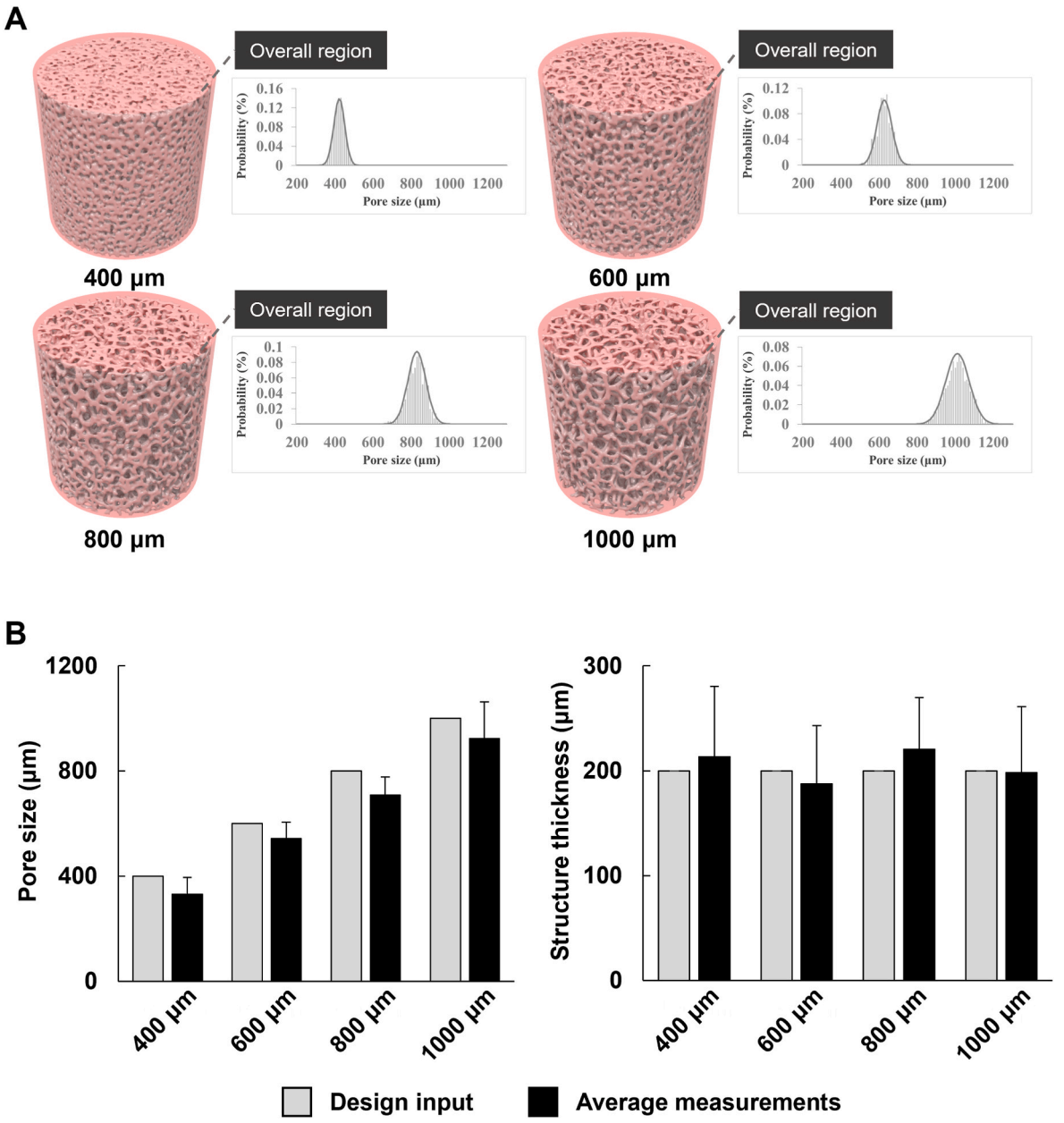

Fig. 1. Structural analysis of porous titanium scaffolds with varying pore sizes (400 μm, 600 μm, 800 μm, 1000 μm); **A.** computer-aided design (CAD) models of scaffolds with highlighted regions in red, where the pore size distribution is analyzed. Accompanying graphs depict the distribution of pore sizes within the highlighted red regions, **B.** comparison of the design input and the actual measured values of pore size and structure thickness.

(1:2000, #H1399, Invitrogen).

To confirm RUNX2 expression, additional Saos-2 samples were prepared by seeding cells on the scaffolds and fixing them after 10 days of culturing. After fixation, the cells were permeabilized and blocked with 3% BSA/PBS for 1 h at room temperature (RT). The cells were then incubated overnight at 4 °C with primary antibody (RUNX2,1:1000, #12556, Cell signaling) diluted in PBS, followed by incubation with the secondary antibody Alexa Fluor™ 488 (1:1000, #A-11008, Invitrogen). For HUVEC cells, VE-cadherin protein visualization was performed by seeding the cells on the scaffolds and fixing them after 7 days of culturing. The primary antibody (VE-cadherin, 1:1000, #ab33168, Abcam) and the secondary antibody (Alexa Fluor™ 488, 1:1000, #A-11008, Invitrogen), both diluted in PBS, were used.

After the staining process, the scaffolds were mounted on the glass bottom dish upside down using a mounting solution (#P36980, Thermo Fisher Scientific). The cells on the titanium scaffold surface were imaged using a fluorescence microscope (DMi8, Leica Microsystems, Germany) with objective lenses of 5x, 10x, and 20× magnification. Additionally, z-stack images were processed using the Leica THUNDER Imager.

2.11. PCR analysis

After incubation of Saos-2 for 7 days on the specimens, total RNA was extracted using NucleoZOL (#740404.200; Macherey-Nacel, Dueren, Germany), in accordance with the manufacturer's instructions. The total RNA concentration was measured using a NanoDrop™ 2000 Spectrophotometer (Thermo Fisher Scientific, Waltham, MA, USA). cDNA was synthesized using RevertAid Reverse Transcriptase (#EP0442; Thermo Fisher Scientific), recombinant RNase inhibitor (#2313A; Takara Bio, Kyoto, Japan), dNTP Mix (#R0192; Thermo Fisher Scientific), Oligo (dT)20 primer (#18418020; Thermo Fisher Scientific), and 1 μg of total RNA. The reaction was performed in a T100 Thermal Cycler (Bio-Rad,

Table 2
Structural features of scaffolds with different pore sizes.

	400 μm	600 μm	800 μm	1000 μm
Porosity	30.6%	43.5%	56.1%	64.0%
Surface area	5053.8 mm^2	4750.4 mm^2	4001.7 mm^2	3356.0 mm^2

Hercules, CA, USA). RT-PCR primers were synthesized by BIONICS (Seoul, Republic of Korea). RT-PCR was performed in a total reaction volume of 25 μL using SYBR Green (#QPS-201; Toyobo, Osaka, Japan) and the CFX Connect™ Real-Time PCR Detection System (Bio-Rad) with the following protocol: initial denaturation at 95 °C for 5 min, followed by 40 cycles of 95 °C for 15 s, 58 °C for 30 s, and 72 °C for 30 s; Glyceraldehyde 3-phosphate dehydrogenase (GAPDH) was used as a control, and mRNA expression levels were normalized by cycle quantification (Cq) of 400 μm specimen. The measurements were repeated 3 times for each experimental condition. The primer sequences are listed in Supplementary Table S2.

2.12. Statistical analysis

Data is presented as means with corresponding standard. To identify

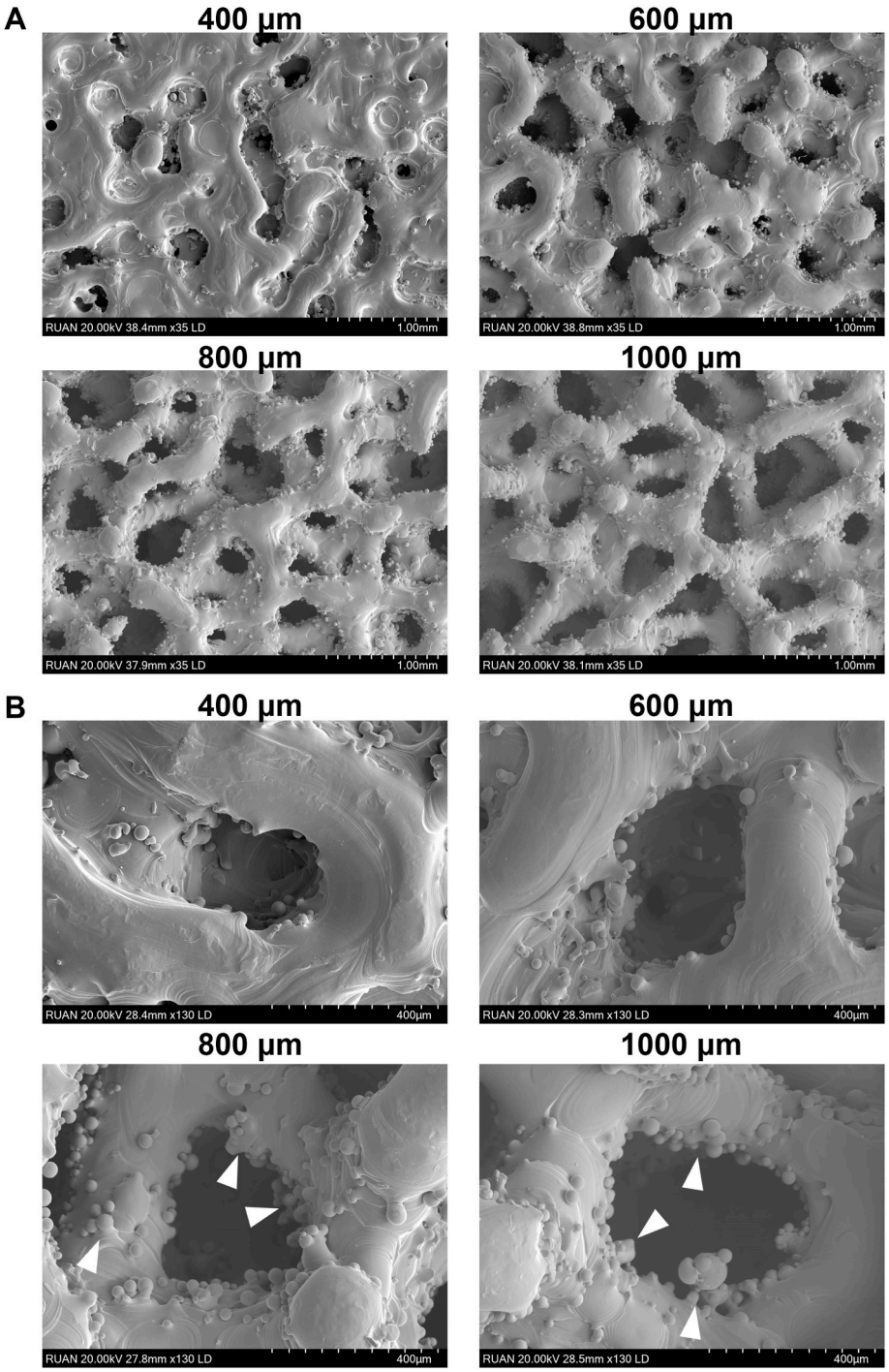

Fig. 2. SEM images of porous titanium scaffolds with varying pore sizes (400 μm, 600 μm, 800 μm, 1000 μm): **A**. low-magnification images at 35x, **B**. high-magnification images at 130x.

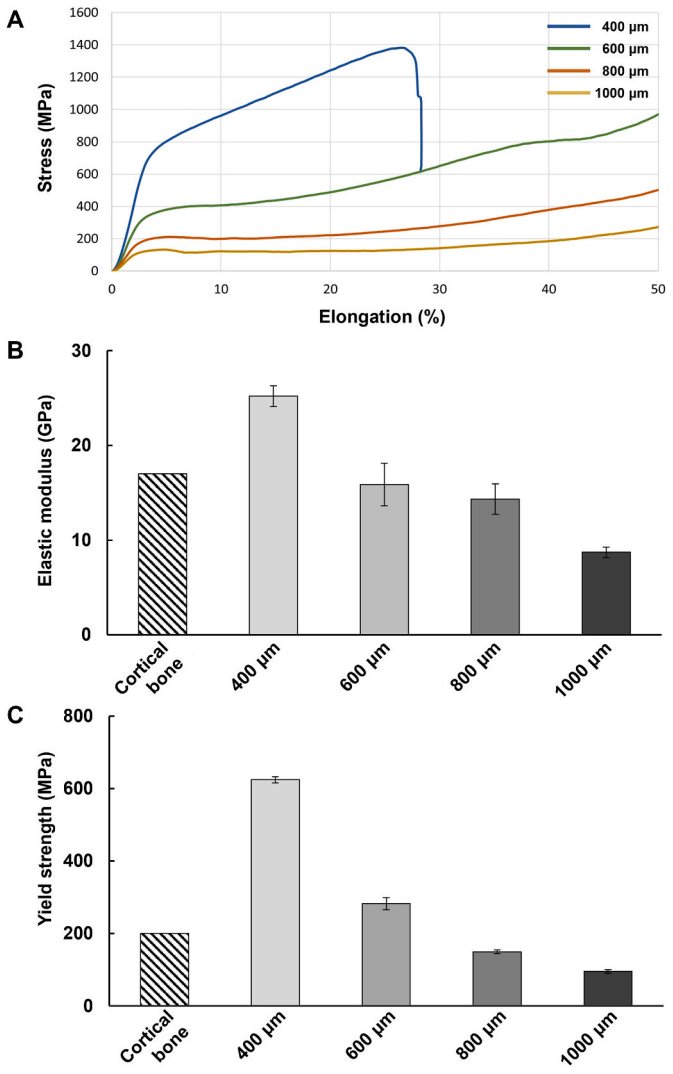

Fig. 3. Mechanical testing results for scaffolds with different pore sizes (400 μm, 600 μm, 800 μm, 1000 μm); **A.** compressive stress-strain curves of scaffolds with various pore sizes, **B.** elastic modulus of scaffolds with different pore sizes (elastic modulus of cortical bone was referred from other's work [42]), **C.** yield strength in scaffolds with different pore sizes (yield strength of cortical bone was referred from other's work [42]).

significant differences between groups, we performed statistical analysis using one-way analysis of variance (ANOVA). Also, for individual data comparison, Tukey post hoc tests were performed. The threshold for statistical significance was set at a P-value of less than 0.05 for all analyses.

3. Result

3.1. Structure analysis through Micro-CT imaging

To verify that the scaffolds were printed with the intended pore sizes of 400 μm, 600 μm, 800 μm, and 1000 μm, Micro-CT imaging was employed to capture the cross-sectional images of each scaffold, and the pore sizes and structural thickness were measured (Fig. 1). The pore sizes slightly deviated from the intended design, appearing approximately 17.3%, 9.7%, 11.6%, and 7.7% smaller than the targeted dimensions in the scaffolds with pore sizes of 400 μm, 600 μm, 800 μm, and 1000 μm, respectively (Fig. 1B). The structure thickness of the printed scaffolds was shown to have an error of approximately 6.8%, 6.3%, 10.3%, and 1.0% from the intended 200 μm thickness in the scaffolds with pore sizes of 400 μm, 600 μm, 800 μm, and 1000 μm, respectively (Fig. 1B). Despite these discrepancies, the overall assessment indicates that the 3D printer successfully fabricated scaffolds according to the design specifications.

From the reconstructed 3D models, the average porosity, and average surface area were analyzed. As can be expected from the pore sizes, specimens with 400 μm pores displayed the lowest porosity, while 1000 μm specimens exhibited the highest porosity (Table 2). As shown in Fig. S7, porosity increases almost linearly with the pore size. In terms of surface area, specimens with 400 μm pores demonstrated the largest surface area, whereas those with 1000 μm pores exhibited the smallest surface area (Table 2).

3.2. Surface characteristics

The surface morphology of scaffolds with different pore sizes were analyzed using SEM, as shown in Fig. 2. The image shows that the pore size increases as the target pore size increases. Scaffolds with 400 μm pores exhibit shallower pores and flatter surfaces compared to those with larger pores. Conversely, scaffolds with larger pores (800 μm and 1000 μm) display more extensive interconnected pore structures compared to scaffolds with smaller pores (400 μm and 600 μm). In addition, scaffolds with 800 μm and 1000 μm pores exhibits a noticeable increase in the number of unmelted particles (indicated with white arrowheads), leading to greater surface roughness than those of smaller pores.

3.3. Material property analysis: elasticity and yield strength

Then, the mechanical properties were assessed, specifically elastic modulus and yield strengths, of the scaffolds with the pore sizes of 400 μm, 600 μm, 800 μm, and 1000 μm. As shown in Fig. 3, there was a clear trend indicating that both the elastic modulus and yield strength decreased as the pore size increased. The elastic modulus was measured to be 25.21 ± 1.1 GPa, 15.88 ± 2.25 GPa, 14.35 ± 1.6 GPa, and 8.72 ± 0.55 GPa for scaffolds with pore sizes of 400 μm, 600 μm, 800 μm, and 1000 μm, respectively. In addition, the yield strength was measured to be 624.3 ± 8.64 MPa, 282.48 ± 17.12 MPa, 149.73 ± 5.41 MPa, and 95.4 ± 5.06 MPa for scaffolds with the corresponding pore sizes. According to previous studies, the elastic modulus and yield strength of human bone are approximately ranging from 0.1 to 17 GPa and 4–200 MPa, respectively [41,42]. Specifically, cortical bones are known to exhibit an elastic modulus from 12 to 17 GPa and a yield strength from 130 to 200 MPa. As depicted in Fig. 3B and C, scaffolds with pore sizes of 600 μm, 800 μm, and 1000 μm closely resemble the mechanical properties of human cortical bone.

3.4. Growth and differentiation characteristics of osteoblasts in relation to pore size

To investigate the growth and differentiation characteristics of osteoblasts in relation to pore size, Saos-2 cells were seeded and cultured on titanium scaffolds with four distinct pore sizes (400, 600, 800, and 1000 μm). Early observations on day 3, shown in Fig. 4A, indicated enhanced cell growth on scaffolds with smaller pore sizes of 400 and 600 μm. Specifically, the mean optical density (O.D.) values of the 400 μm and 600 μm scaffolds were 38.2% and 67.4% higher, respectively, compared to those of the 800 μm scaffolds, and 53.9% and 86.5% higher, respectively, compared to those of the 1000 μm scaffolds. However, a contrasting trend emerges by the 10 and 14-day marks, where scaffolds featuring larger pores—specifically those with a pore size of 1000 μm—showed significantly better cell proliferation than those with smaller pores. By day 14, the mean O.D. value for the 1000 μm scaffolds was 51.3%, 17.2%, and 11.9% higher than that of the 400, 600, and 800 μm scaffolds, respectively.

This observed trend in cell proliferation was reflected in the

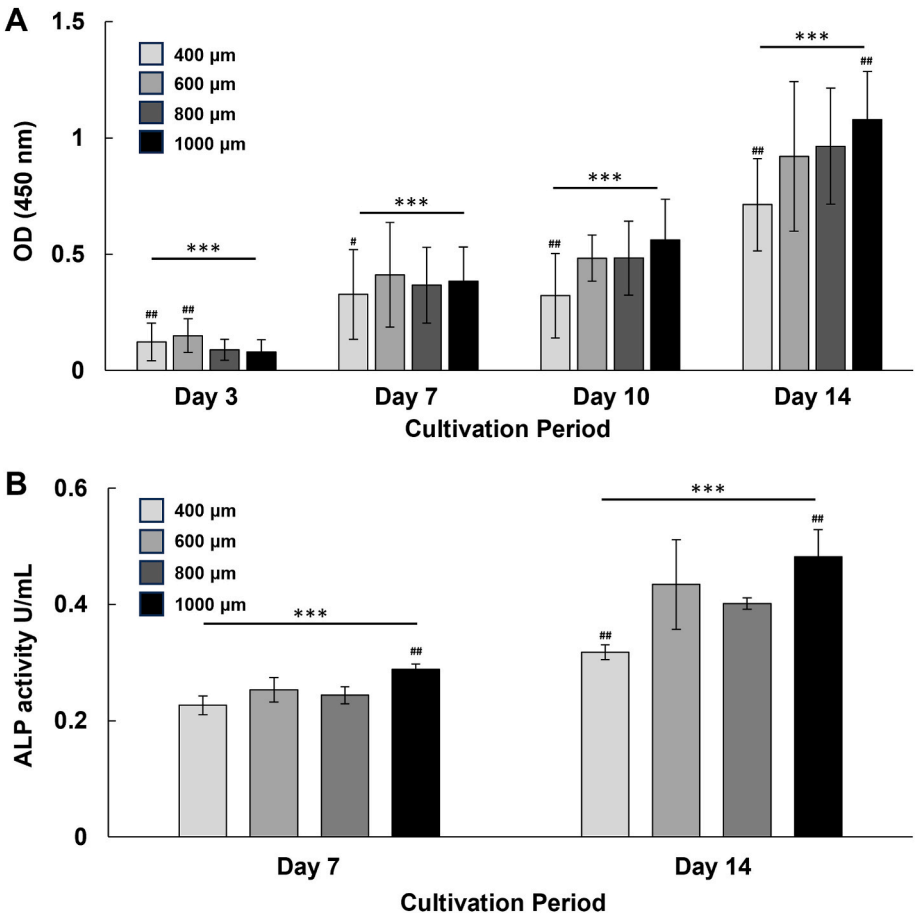

Fig. 4. Proliferation and differentiation of Saos-2 cells on scaffolds with different pore sizes (400 µm, 600 µm, 800 µm, 1000 µm); **A**. Saos-2 proliferation measured by optical density at 450 nm (OD) on days 3, 7, 10, and 14 using the CCK-8 assay, **B.** alkaline phosphatase (ALP) activity measured on days 7 and 14. (One-way ANOVA: ***P $<$ 0.001, Tukey post hoc test: $^{\#}$P $<$ 0.05, $^{\#\#}$P $<$ 0.05).

differentiation characteristics of the cells. As alkaline phosphatase (ALP) enzyme is one of the representative markers of osteoblast differentiation [43,44]. ALP activity was measured on days 7 and 14, as shown in Fig. 4B. It was shown that cells cultured on scaffolds with 1000 µm pores exhibited the highest ALP activity, whereas those on scaffolds with 400 µm pores displayed the lowest activity. Notably, on day 14, the ALP activity of scaffolds with 1000 µm pores increased by approximately 27.6% compared to those with 400 µm pores.

To further evaluate gene expression related to osteogenic differentiation, we performed PCR to analyze COL1, OPN, and OCN in Saos-2 cells cultured on scaffolds with pore sizes of 400 µm and 1000 µm. These pore sizes were selected from the four conditions (400, 600, 800, and 1000 µm) as they demonstrated the most pronounced differences in cell proliferation and differentiation. As shown in Fig. S8, the relative mRNA expression levels of COL1 and OPN did not show statistically significant differences between the two pore sizes. However, the expression of OCN in the 1000 µm scaffolds increased approximately fivefold compared to the 400 µm scaffolds.

As confirmed above, in terms of osteoblast proliferation and differentiation, our observations suggest a superior performance in scaffolds with larger pore sizes compared to those with smaller pores. We, then, utilized fluorescent immunostaining to assess the spatial distribution of adhering cells on the scaffold. In Fig. 5, a series of images depicts the nucleus in grayscale in the first column, actin stress fibers in the second column, and the merged image of the nucleus (blue) and actin (red) in the third column. Upon comparison of cells on scaffolds with pore sizes of 400, 600, 800, and 1000 µm to those on smooth surface, it is evident that the cells are distributed in three dimensions, resulting in out-of-focus cells. In the nucleus and actin images, white dashed lines are used to highlight cells within the pores. The depth of pores appears to be greater in the scaffolds with larger pore sizes, specifically 800 and 1000 µm. While the majority of cells seem to be evenly distributed on the surface, there are occasional areas where cells heavily clump together, as indicated by white arrowheads in the high-resolution image in Fig. S9. Overall, the distribution of cells on the scaffold surface area does not appear to differ significantly across different pore sizes.

To better understand the influence of local topography on osteoblast differentiation, we examined the expression of RUNX2, an early marker of osteoblast differentiation [43]. To assess its distribution in relation to surface topography, cells were fixed and stained at an earlier time point compared to the above experiments, which were conducted at day 14 of cell culture. Saos-2 cells were cultured on scaffolds with varying pore sizes (400 µm, 600 µm, 800 µm, and 1000 µm) for 10 days. Immunostaining for RUNX2 revealed that, while overall RUNX2 expression was consistent across all pore sizes, closer examination of the scaffold surfaces showed distinct patterns influenced by local topography. Specifically, cells adhering to rough areas of the scaffold, particularly regions with unmelted particles, exhibited higher RUNX2 expression (Fig. 6). The red dotted circles in the enlarged images in Fig. 6 highlight areas with unmelted particles, where more cells were observed to accumulate, displaying stronger RUNX2 fluorescence signals compared to the surrounding regions (indicated with white arrowheads).

3.5. Growth characteristics of endothelial cells in relation to pore size

Subsequently, we explored the proliferation of endothelial cells on

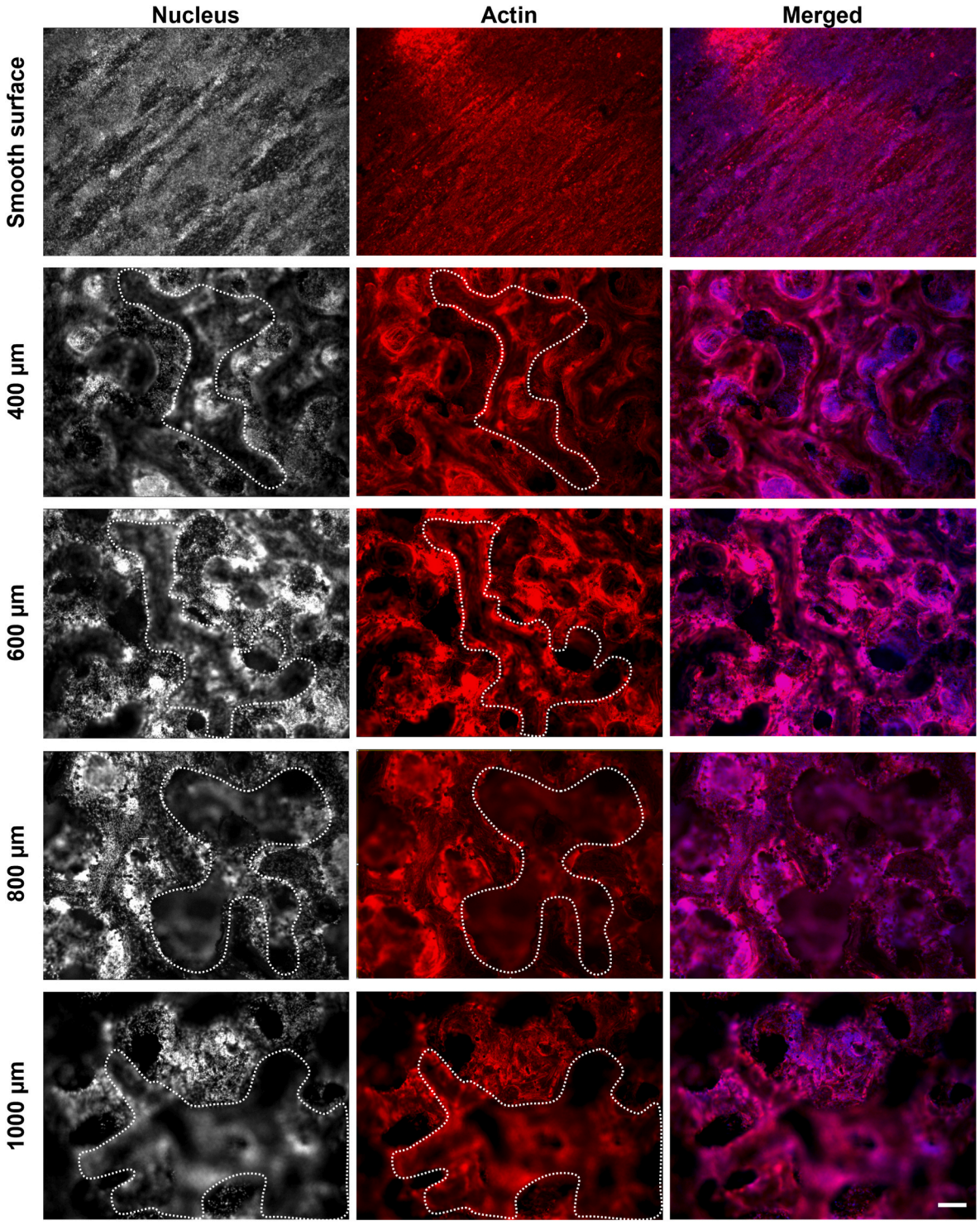

Fig. 5. Immunofluorescence image of Saos-2 cells on scaffolds with different pore sizes (400 µm, 600 µm, 800 µm, 1000 µm). Images show nuclei in gray (Hoechst 33342) in the first column, actin stress fibers in red (phalloidin) in the second column, and merged images of the nucleus (blue) and actin (red) in the third column. Cells within the pores are marked by white dashed lines. [Scale bar = 250 µm].

scaffolds with varying pore sizes to assess their impact on neovascularization, a critical process for bone healing and regeneration. For that, we used HUVEC as this is widely recognized as a reliable and well-characterized primary cell type for in vitro studies of angiogenesis [45–47]. Intriguingly, the results for HUVECs differed markedly from those observed with osteoblasts. As shown in Fig. 7, from the early stage on day 3 and continuing through days 7, 10, and 14, HUVECs exhibited the highest proliferation rates on scaffolds with the smallest pore size of 400 µm. Conversely, scaffolds with the largest pore size of 1000 µm showed the lowest HUVEC proliferation. On scaffolds with intermediate pore sizes of 600 µm and 800 µm, proliferation increased gradually but was still less than that seen with the 400 µm scaffolds. In particular, the mean O.D. value of the 400 µm scaffold was 22.3%, 103.4%, and 137.3% higher than those of the 600 µm, 800 µm, and 1000 µm scaffolds, respectively (Fig. 7).

To further investigate the influence of pore size and the resulting

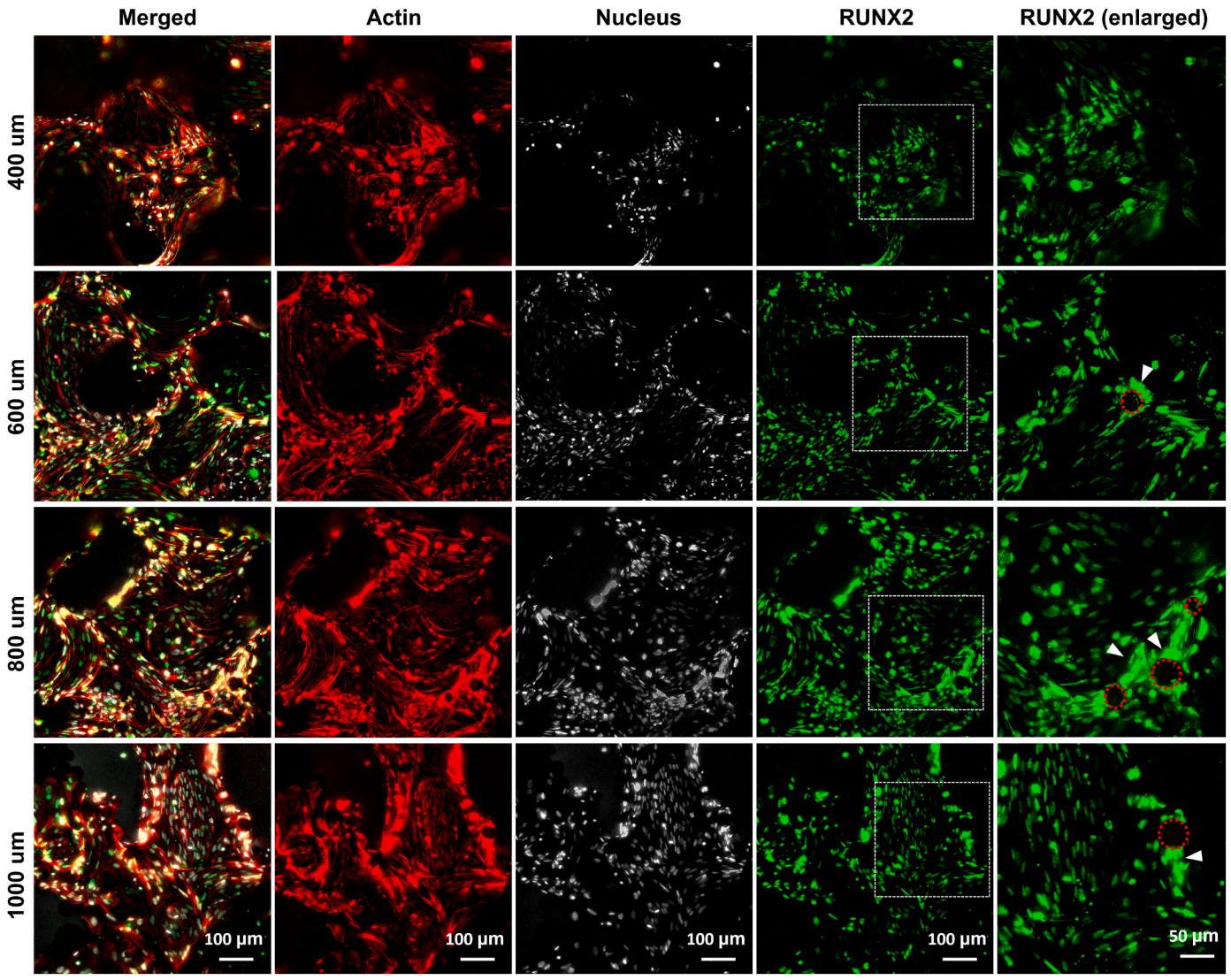

Fig. 6. Immunofluorescence images of Saos-2 cells on scaffolds with pore sizes of 400 µm, 600 µm, 800 µm, and 1000 µm. Z-stack images processed and shown as z-projections using Leica image acquisition software (Thunder Imager, Leica). First column: merged images; second column: actin stress fibers (red); third column: nuclei (gray); fourth column: RUNX2 (green). Regions in white dashed boxes (fourth column) are enlarged in the fifth column. Unmelted particles indicated with red dotted circles. [Scale bars = 100 µm (columns 1–4) and 50 µm (column 5)].

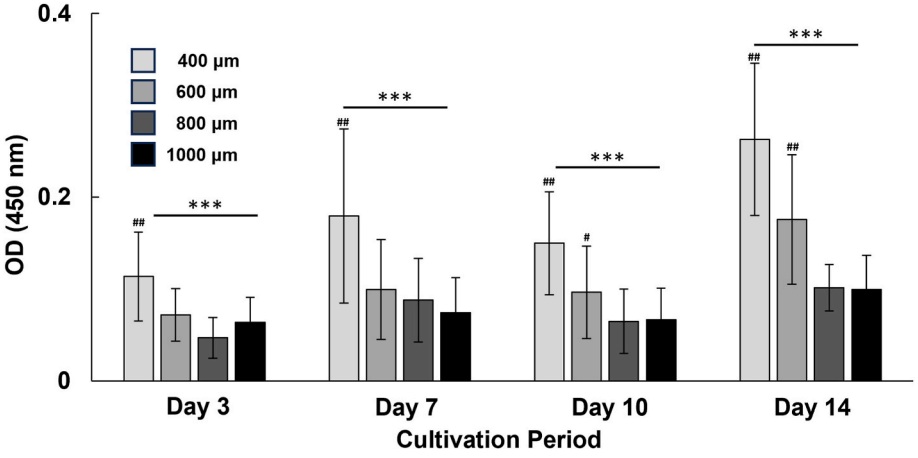

Fig. 7. Proliferation of HUVECs on scaffolds with different pore sizes (400 µm, 600 µm, 800 µm, 1000 µm): HUVEC proliferation was quantified at days 3, 7, 10, and 14 using the CCK-8 assay. (One-way ANOVA: ***$P < 0.001$, Tukey post hoc test: $^{\#}P < 0.05$, $^{\#\#}P < 0.05$).

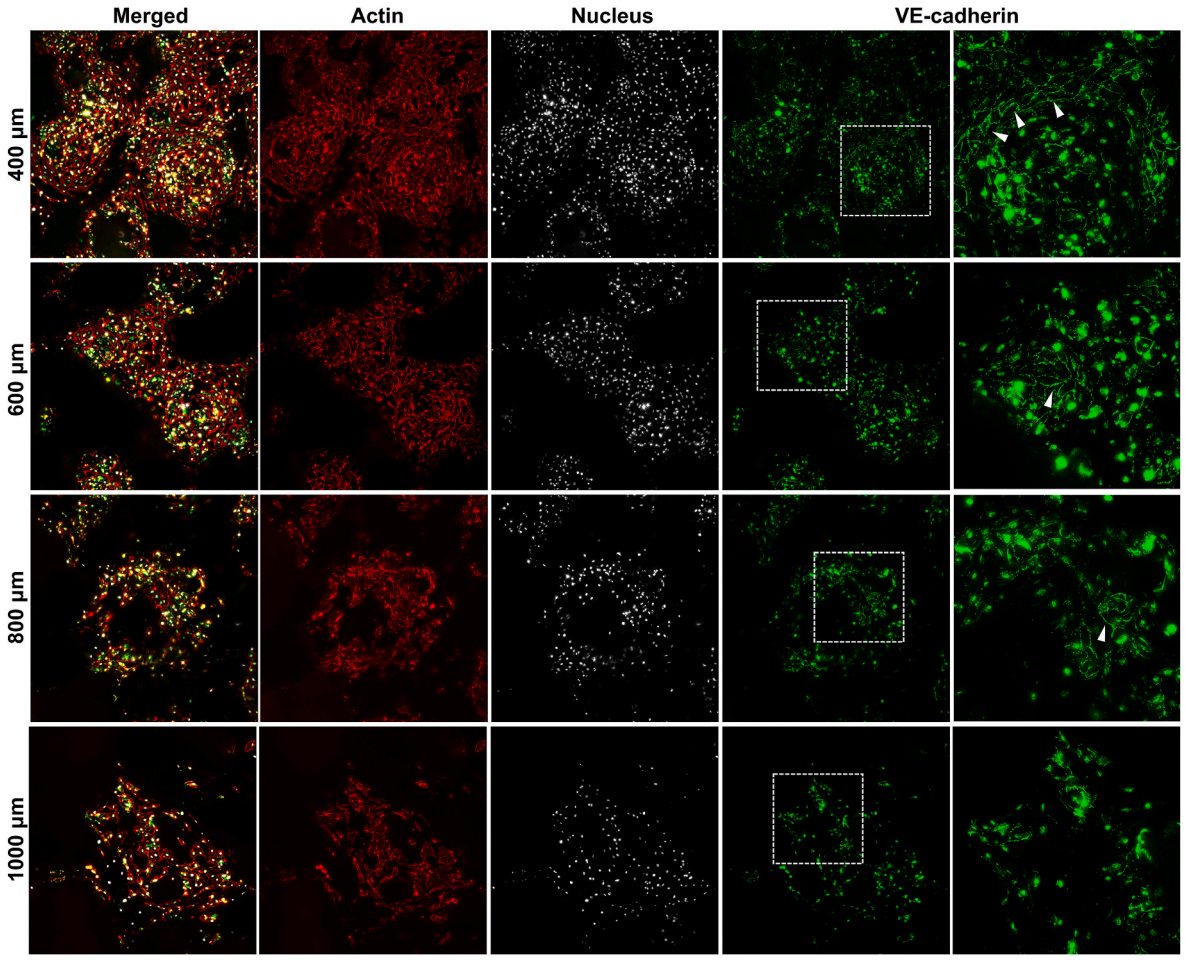

Fig. 8. Immunofluorescence images of HUVEC cells on scaffolds with pore sizes of 400 µm, 600 µm, 800 µm, and 1000 µm. Z-stack images processed and shown as z-projections using Leica image acquisition software (Thunder Imager, Leica). First column: merged images; second column: actin stress fibers (red); third column: nuclei (gray); fourth column: VE-cadherin (green). Regions in white dashed boxes (fourth column) are enlarged in the fifth column. [Scale bars = 200 µm (columns 1–4) and 80 µm (column 5)].

scaffold structure on endothelial cell behavior, VE-cadherin, a critical endothelial cell adhesion molecule essential for vascular development [48], was labeled as a marker for vessel formation. As shown in Fig. 8, the number of cells decreased with increasing pore size, aligning with the observed proliferation trends described earlier. Cells were predominantly localized within the pores and along their peripheries. In scaffolds with larger pores (800 µm and 1000 µm), cells were primarily observed at the periphery and failed to form a continuous monolayer, instead exhibiting incomplete and sparsely distributed cell layers. In contrast, scaffolds with smaller pores (400 µm and 600 µm) supported higher cell density, resulting in more cohesive and complete endothelial layers across the scaffold surfaces. This enhanced cell coverage appears to contribute to the observed increase in VE-cadherin expression (indicated with white arrowheads in the enlarged images in Fig. 8).

3.6. Structure analysis of scaffolds with a gradient of pore sizes

The evaluation of the material properties of the scaffolds revealed that scaffolds with pore sizes ranging from 600 to 1000 µm manifested characteristics closely resembling natural human bone. However, in terms of the proliferation and differentiation of osteoblasts, the scaffold with a pore size of 1000 µm yielded the most superior outcomes. Conversely, with regard to the endothelial cells, the scaffold with the smallest pore size of 400 µm demonstrated the best proliferation. Considering these aspects collectively, it appears that there is no universally optimal pore size for concurrently enhancing mechanical properties, osteointegration, and vascularization simultaneously.

Therefore, we pursued a scaffold design that incorporated a range of pore sizes to accommodate all these functionalities. This led to a gradient of pore sizes, ranging from small (400 µm) to large pores (1000 µm). Fig. 9A depicts two types of gradients: in Type1, the gradient starts from the lower portion and extends towards the upper portion of the scaffolds; in Type 2, the gradient starts from the peripheral region and extends towards the center. In Type 1, when examining the side of the scaffold, the pores are smaller at the bottom and gradually increase in size towards the top. In Type 2, when observing the top of the scaffold, the pores are smaller at the outside and gradually increase in size towards the center (Fig. 9A).

Then, to confirm whether the printed scaffolds adhered to the intended design, pore size and structure thickness were validated through 3D models reconstructed from micro-CT cross-sectional images. Following the design specifications, which define the pore size in the area where the gradient starts and ends, but not in the intermediary region, measurements of pore size and structure thickness were conducted in the regions marking the starting and ending points of the gradient. As shown in Fig. 9B, the actual pore sizes of the scaffolds were smaller than the intended design. Specifically, the pore sizes at the bottom and top of the Type 1 scaffold were approximately 6.8% and 5.4% smaller than the targeted sizes of 400 µm and 1000 µm, respectively. Similarly, for the Type 2 scaffold, the pore sizes at the periphery and center were 10.5% and 3.2% smaller than the targeted dimensions of 400 µm and 1000 µm, respectively (see Fig. 9B). The thickness of the

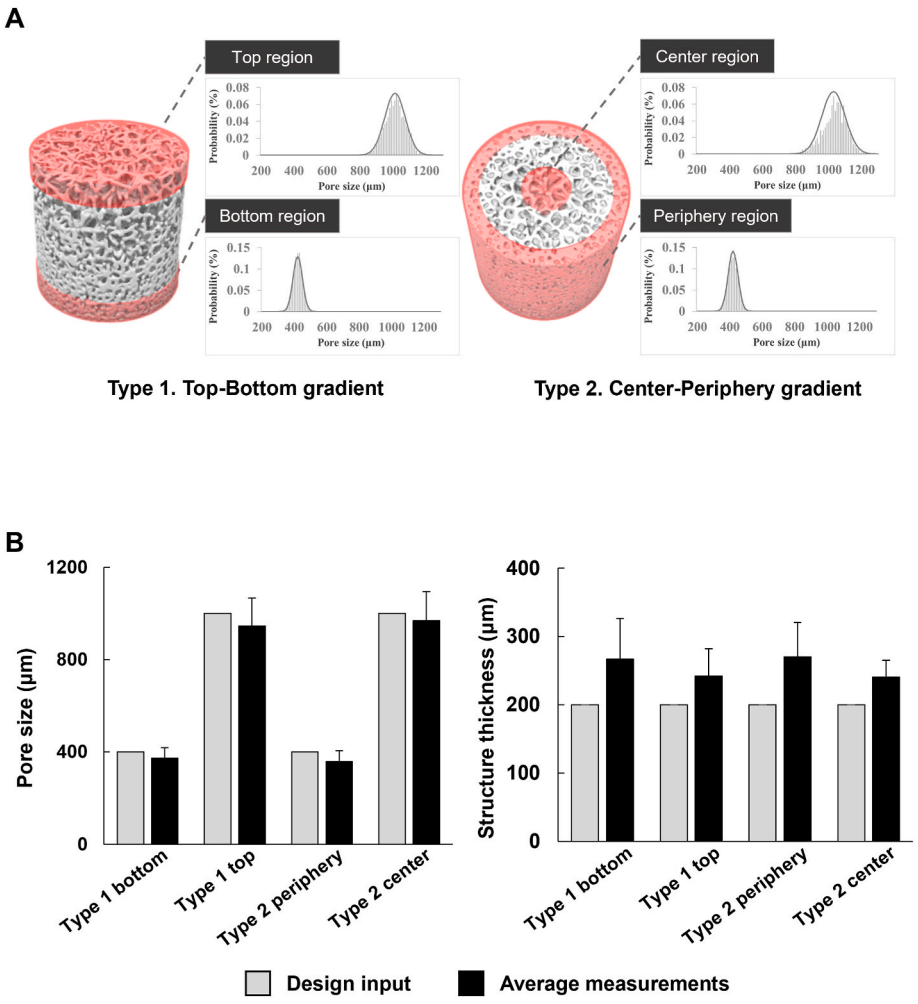

Fig. 9. Structural analysis of pore size-gradient scaffolds (Type 1: Top-Bottom gradient, and Type 2: center-periphery gradient); **A.** Computer-aided design (CAD) models of scaffolds with highlighted regions in red, where the pore size distribution is analyzed. Accompanying graphs depict the distribution of pore sizes within the highlighted red regions, **B.** comparison of the design input and the actual measured values of pore size and structure thickness.

Table 3
Structural features of Type 1 and Type 2 scaffolds.

	Type 1		Type 2	
	Top	Bottom	Center	Periphery
Porosity	21.2%	64.6%	19.8%	62.3%
Surface area	4420.7 mm^2		4702.6 mm^2	

printed scaffolds deviated from the intended 200 μm by approximately 33.5%, 21.0%, 35.0%, and 20.3% for the scaffolds with pore sizes of 400 μm (Type 1 bottom), 1000 μm (Type 1 top), 400 μm (Type 2 periphery), and 1000 μm (Type 2 center), respectively (Fig. 9B). As shown in previous results with scaffolds ranging in size from 400 to 1000 μm, slight discrepancies exist between the measured pore sizes and structure thickness and the intended design, but the overall results confirm that the scaffolds were fabricated according to the targeted design for both Type 1 and Type 2 scaffolds. Additionally, the porosity and total surface area of each scaffold were measured, as shown in Table 3 below.

3.7. Material property analysis of the scaffolds with a gradient in pore sizes

We then investigated how the elastic modulus and yield strength would be affected by the gradient of pore size and by the direction of the gradients. The tested scaffolds are shown in Fig. S6. The force applied during the mechanical test was directed vertically, compressing the cylindrical specimen from the top and bottom (Fig. S4). Therefore, the mechanical properties of Type 1 and Type 2 seem to vary depending on the orientation of the gradient in relation to this applied force direction. As shown in Fig. 10, both the elastic force and yield strength were greater for Type 2 than for Type 1. The elasticity was measured as 10.82 ± 1.73 MPa for Type 1 and 18.68 ± 3.1 MPa for Type 2, while the yield strength was measured as 151.52 ± 6.08 MPa for Type 1 and 388.13 ± 25.83 MPa for Type 2. Compared to the scaffolds with single pore sizes shown in Fig. 3, Type 1 scaffold exhibits an elastic force or yield strength comparable to that of a scaffold with a 1000 μm pore size, while Type 2 scaffold demonstrates an elastic force or yield strength akin to a scaffold with a 600 μm pore size.

The difference in mechanical properties between Type 1 and Type 2 scaffolds arises from the alignment of the gradient relative to the direction of the applied mechanical force. For Type 1 scaffold, the gradient is oriented parallel to the axis of the applied force. As a result, under compression, the mechanical behavior is predominantly governed by the properties of the large pores (1000 μm), leading to a similar elastic modulus and yield strength as that of the large pores. In contrast, Type 2 scaffold features a gradient oriented perpendicular to the axis of the applied force. This perpendicular arrangement results in a more uniform distribution of stress across both the small (400 μm) and large pores (1000 μm). Consequently, Type 2 scaffolds exhibit intermediate elastic

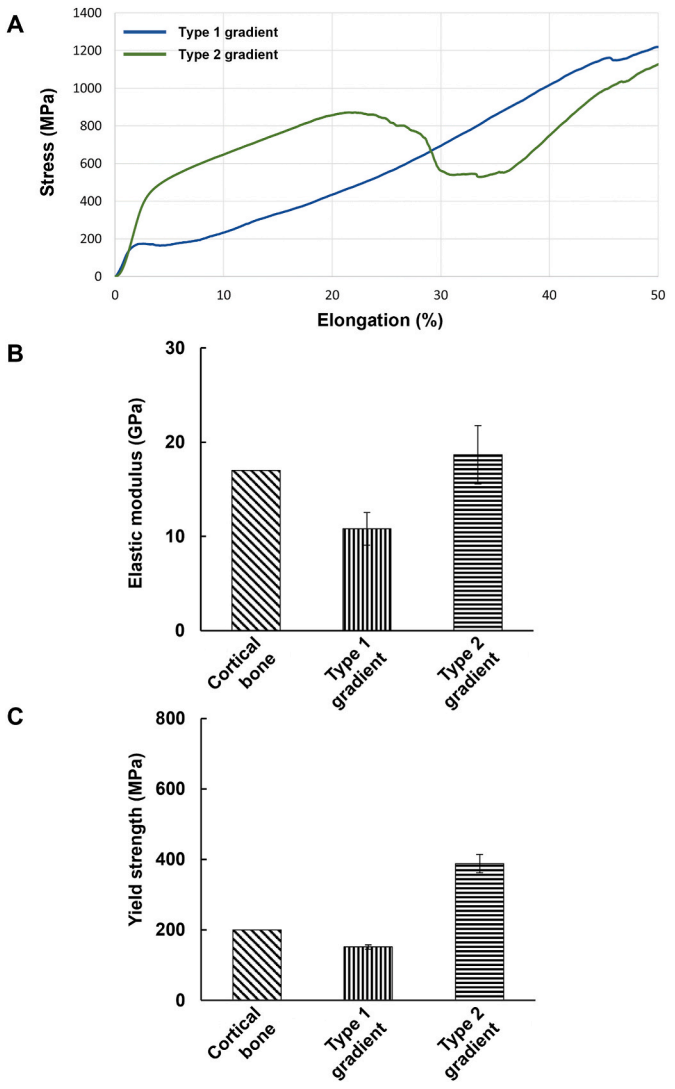

Fig. 10. Mechanical testing results for pore size-gradient scaffolds (Type 1: Top-Bottom gradient, and Type 2: center-periphery gradient); **A.** compressive stress-strain curves, **B.** elastic modulus, and **C.** yield strength of scaffolds of Type1 and Type 2 scaffolds (elastic modulus and yield strength of cortical bone was referred from other's work [42]).

modulus and yield strength values that reflect the combined contributions of the small and large pores. Importantly, it is worth noting that both the Type 1 and Type 2 scaffolds possess an elastic modulus similar to that of human cortical bone.

3.8. Impact of pore-size-gradient to osteoblasts and HUVEC

We then conducted in vitro experiments employing Saos-2 to examine how the gradient in pore sizes affects the growth of osteoblasts. To compare Saos-2 cell proliferation characteristics on Type 1 and Type 2 scaffolds with those exhibiting the lowest (400 μm) and the highest (1000 μm) cell proliferation characteristics, we simultaneously seeded cells on Type 1, Type 2, 400 μm, and 1000 μm scaffolds.

Interestingly, osteoblasts demonstrated an accelerated proliferation profile in both Type 1 and Type 2 gradient scaffolds compared to the 400 μm scaffold (Fig. 11A). Particularly in Type 2, the proliferation rate of Saos-2 was high at the early cultivation time point (day 3, and 7), and this trend persisted until the late cultivation time point (day 14) (Fig. 11A). The proliferation characteristics observed on day 14 are comparable to those seen in the 1000 μm scaffold, which exhibited the highest proliferation. These results indicate that the combination of different pore sizes ranging from 400 μm to 1000 μm was substantially advantageous for osteoblast proliferation. Additionally, ALP assay was employed to assess and compare cell differentiation across different scaffolds. According to Fig. 11B, in Type 1 scaffolds, ALP activity was similar to that of 400 μm scaffolds. Conversely, in Type 2 scaffolds, ALP activity closely resembled that of 1000 μm scaffolds, which exhibited the highest level of ALP activity. Hence, these results confirm that Type 2 scaffolds feature characteristics that facilitate both proliferation and differentiation of osteoblasts.

Subsequently, the proliferation characteristics of endothelial cells were also measured using HUVECs. As corroborated in Fig. 7, in contrast to Saos-2, HUVECs demonstrated the most favorable proliferation on scaffolds featuring a pore size of 400 μm, while exhibiting the lowest proliferation levels on scaffolds with a pore size of 1000 μm. In Fig. 11C, in Type 1 scaffolds, cell proliferation was observed to be similar to 1000 μm scaffolds. However, Type 2 scaffolds exhibited significantly higher cell proliferation compared to Type 1 and 1000 μm scaffolds. Although the proliferation of HUVECs in Type 2 scaffolds was 21.7% less than that in 400 μm scaffolds at a 14-day period, it still showed a notable improvement compared to both Type 1 and 1000 μm scaffolds.

Collectively, considering the proliferation and osteogenic differentiation characteristics of osteoblasts, along with the proliferation of vascular endothelial cells, Type 2 scaffolds appear to manifest the most favorable characteristics for facilitating osteointegration.

4. Discussion

Our study emphasizes the essential role of pore size and its spatial distribution in porous scaffolds in enhancing biomechanical compatibility and biological performance. We found that optimal pore sizes differed depending on the specific function targeted, such as mechanical properties, osteoblast behavior, or endothelial cell activity. Notably, the observed influence of pore size can also be interpreted as the effect of porosity, as porosity increases linearly with pore size (Fig. S7), impacting both mechanical properties and cellular responses. Based on these findings, we hypothesized that scaffolds incorporating a gradient in pore sizes could synergistically enhance both biomechanical and biological functions. Through subsequent experiment, we were able to confirm this hypothesis that a gradient in pore sizes, as exemplified by the Type 2 scaffolds, can effectively balance the biomechanical compatibility with native bone tissue while optimizing osteointegration and vascularization.

As shown in our results, the initial in vitro investigation using scaffolds with various pore sizes (400, 600, 800, and 1000 μm) manifested distinct proliferation patterns between osteoblast-like cells (Saos-2) and endothelial cells (HUVECs) with respect to pore sizes. Saos-2 cell proliferation notably thrived at the largest pore size of 1000 μm, which is consistent with previous reports suggesting the advantages of relatively large pores for osteointegration [23,24,27]. Interestingly, our results also revealed that the scaffolds with smaller pores (400 and 600 μm) facilitated proliferation of Saos-2 cells at early time points (days 3 and 7), highlighting their critical role in early-stage cell recruitment. As the culture period extended, scaffolds with large pores (1000 μm) demonstrated a marked increase in cell proliferation and differentiation, particularly evident on days 10 and 14, which indicates their role in promoting sustained osteogenic activity. Thus, incorporating a gradient in pore sizes within the scaffolds harmonized these benefits, leading to consistently superior proliferation throughout the entire culture period from day 3 to day 14. Once again, this reinforces the potential of functionally graded pore structures in optimizing scaffold performance for both immediate cellular response and long-term tissue integration.

Conversely, endothelial cells proliferated most actively in scaffolds with the smallest pore size of 400 μm compared to larger counterparts (600, 800, and 1000 μm). Previous studies on endothelial cells have reported contrasting results regarding pore size preferences; some

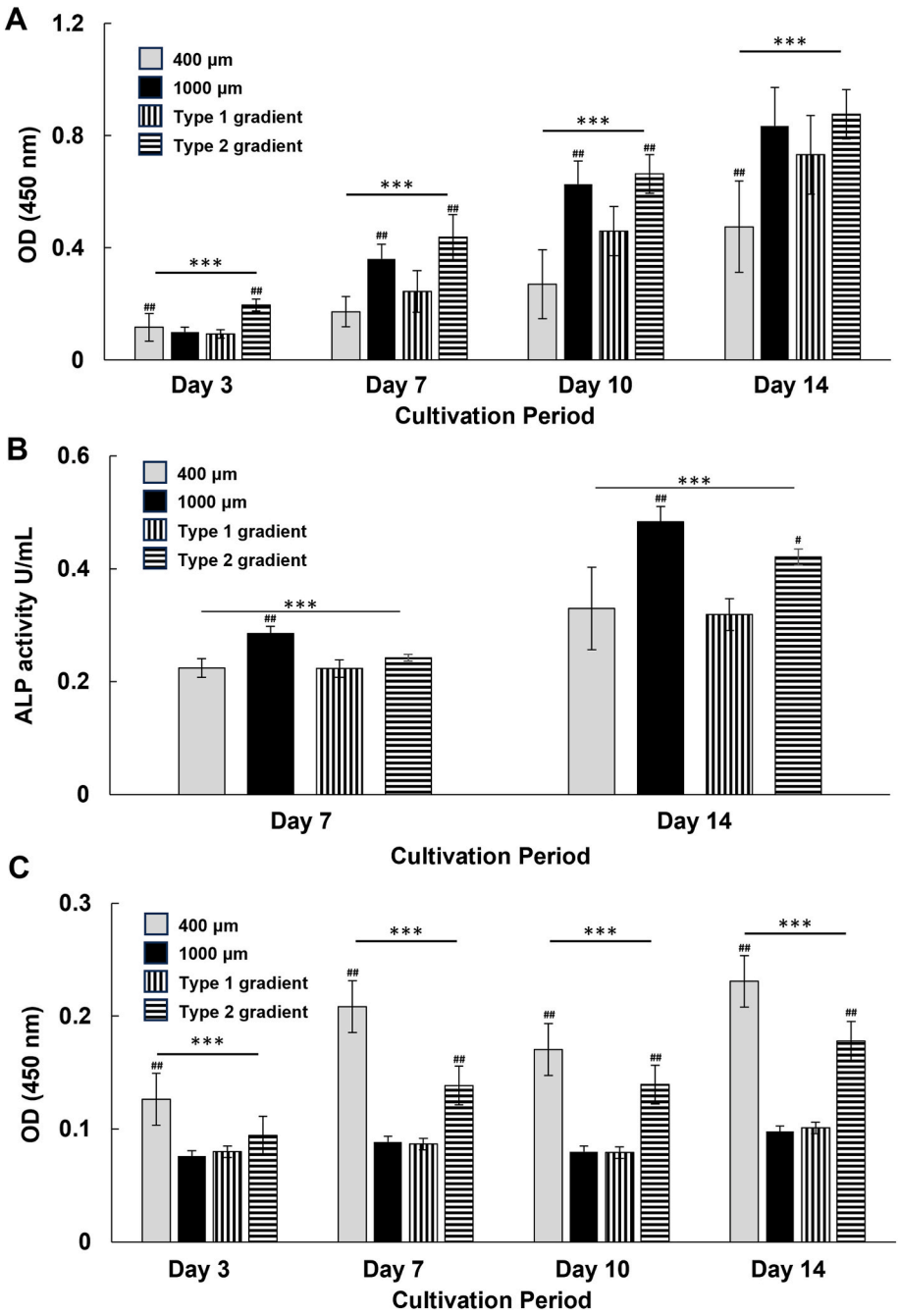

Fig. 11. Cellular responses to 400 µm, 1000 µm, Type 1, and Type 2 scaffolds: center-periphery gradient); **A**. Saos-2 proliferation measured on days 3, 7, 10, and 14, **B.** alkaline phosphatase (ALP) activity on days 7 and 14. **C**. HUVEC proliferation quantified at days 3, 7, 10, and 14. (One-way ANOVA: ***P < 0.001, Tukey post hoc test: $^{\#}P < 0.05$, $^{\#\#}P < 0.05$).

researchers suggested that larger pore sizes foster better vascularization [37,38], while others argued in favor of smaller pore sizes [39,49]. Therefore, while some studies aligned with our results, others demonstrated opposing results; however, direct comparisons may be difficult due to differences in scaffold materials, fabrication methods, and pore size ranges across these studies compared to ours. Nevertheless, the study by Choi et al. is noteworthy, which showed that large vessels with deep penetration depth were formed more effectively in scaffolds with larger pore sizes, whereas smaller vessels with high density were formed in scaffolds with smaller pore sizes [40]. In this context, the existence of contrasting studies is understandable, and it can be expected that our gradient-based scaffold design has the potential to accommodate both large and small vessel formation, offering significant advantages in supporting tissue regeneration, including bone regeneration.

The findings for Saos-2 and HUVEC cells are individually intriguing, but the differences in their responses based on cell type are particularly noteworthy. As discussed above, Saos-2 cells demonstrated superior proliferation on scaffolds with larger pore size (1000 µm), whereas HUVEC cells exhibited enhanced growth on scaffolds with smaller pore size (400 µm). Fig. 6 and S9 demonstrate that Saos-2 cells preferentially accumulate on rough and convoluted surfaces and can form dense clusters as their population increases. In contrast, HUVEC cells preferred flat and shallow pores, where they can develop more cohesive and intact endothelial layers (Fig. 8). These observations align with the SEM images shown in Fig. 2, which exhibit the structural differences between the scaffolds. The 400 µm scaffolds are characterized by shallower pores

and broader, flatter surfaces. In contrast, the 1000 μm scaffolds feature rougher, more convoluted surfaces with a higher density of unmelted particles and deeper pores. These structural differences likely explain the distinct preferences of each cell type for specific microenvironments, particularly with respect to surface roughness. This, in turn, leads to the observed variations in their proliferation and differentiation patterns. These findings highlight the advantages of Type 2 gradient scaffolds, which integrate diverse microenvironmental features present in both the 400 μm and 1000 μm scaffolds. Such scaffolds provide an ideal platform for supporting the growth of both bone-forming cells (osteoblasts) and vascular cells (endothelial cells), ultimately promoting effective osteointegration.

In addition to the biological superiority of the Type 2 gradient scaffolds, questions may arise regarding the observed discrepancies between the Type 1 and Type 2 scaffolds. Based on our observations and the scaffold design, it is likely that cells predominantly attach to the top surface during the initial seeding phase. For Type 1 gradient scaffolds, the top surface features structural characteristics similar to the 1000 μm scaffolds due to the gradient direction, which may explain why Type 1 scaffolds demonstrated biological responses more closely resembling those of the 1000 μm scaffolds. In contrast, the top surface of Type 2 scaffolds integrates diverse microenvironmental features from both the 400 μm and 1000 μm scaffolds. This integrated design likely accounts for the distinct biological outcomes observed between Type 1 and Type 2 scaffolds.

In summary, our biological data, based on in vitro experiments, provide critical insights into cellular responses to scaffold designs. Previous studies have shown that superior in vitro outcomes often translate to enhanced in vivo performance [22,50,51]. Thus, we believe our in vitro findings establish a strong foundation to anticipate the potential benefits of these scaffolds for bone ingrowth and integration in vivo. However, further studies are needed to confirm these benefits and understand the key factors for translating these findings into practical applications.

Furthermore, considering the heterogeneous density and mechanical properties of the cortical and cancellous bone in natural bone, the use of gradient pore sizes may offer more biomechanically favorable designs for implants. By aligning scaffold designs with the density and mechanical properties of adjacent bone tissues, we can potentially enhance the biomechanical compatibility and long-term stability of bone implants. Additional longitudinal in vivo studies are necessary to further validate these findings and to explore the long-term stability and biocompatibility of the implants.

5. Conclusion

In summary, this study proposed a titanium scaffold design featuring gradients in pore sizes ranging from 400 to 1000 μm. These scaffolds, fabricated with PBF technology, exhibited notable improvement in both their biomechanical and biological performance through in vitro experiments. This dual optimization strategy is particularly beneficial for bone tissue engineering applications, where the simultaneous delivery of mechanical support and biological functionality is essential. We believe that by finely tuning the pore sizes and further aligning them with the adjacent bone structures, we can greatly enhance the performance of bone implants.

CRediT authorship contribution statement

Ara Jung: Methodology, Formal analysis, Investigation, Data curation, Writing – original draft. **Jinju Jang:** Software, Formal analysis, Investigation, Visualization, Writing – original draft. **Hun Yeong Ban:** Conceptualization, Data curation, Software. **Hee Jin Kim:** Formal analysis, Investigation. **Bomi Gweon:** Conceptualization, Data curation, Writing – original draft, Writing – review & editing, Resources, Supervision, Funding acquisition. **Dohyung Lim:** Conceptualization, Data curation, Writing – review & editing, Resources, Supervision, Funding acquisition.

Data availability

The datasets generated during and/or analyzed used during the current study are available from corresponding authors upon reasonable request.

Declaration of competing interest

The authors declare that they have no known competing financial interests or personal relationships that could have appeared to influence the work reported in this paper.

Acknowledgements

This work was supported in part by the NRF Grant funded by the Korean Government (NRF-2022R1A2C2010940) and by the Korea Medical Device Development Fund grant funded by the Korea government (the Ministry of Science and ICT, the Ministry of Trade, Industry and Energy, the Ministry of Health & Welfare, and the Ministry of Food and Drug Safety) (RS-2020-KD000038).

Appendix. ASupplementary data

Supplementary data to this article can be found online at https://doi.org/10.1016/j.jmrt.2024.12.216.

References

[1] Kurtz S, Ong K, Lau E, Mowat F, Halpern M. Projections of primary and revision hip and knee arthroplasty in the United States from 2005 to 2030. J Bone Joint Surg Am 2007;89(4):780–5.
[2] Harwin SF, Elmallah RK, Jauregui JJ, Cherian JJ, Mont MA. Outcomes of a newer-generation cementless total knee arthroplasty design. Orthopedics 2015;38(10):620–4.
[3] Mont MA, Gwam C, Newman JM, Chughtai M, Khlopas A, Ramkumar PN, Harwin SF. Outcomes of a newer-generation cementless total knee arthroplasty design in patients less than 50 years of age. Ann Transl Med 2017;5(Suppl 3):S24.
[4] Filip N, Radu I, Veliceasa B, Filip C, Pertea M, Clim A, Pinzariu AC, Drochioi IC, Hilitanu RL, Serban IL. Biomaterials in orthopedic devices: current issues and future perspectives. Coatings 2022;12(10).
[5] Ryu DJ, Ban HY, Jung EY, Sonn CH, Hong DH, Ahmad S, Gweon B, Lim D, Wang JH. Osteo-compatibility of 3D titanium porous coating applied by direct energy deposition (DED) for a cementless total knee arthroplasty implant: in vitro and in vivo study. J Clin Med 2020;9(2).
[6] Karageorgiou V, Kaplan D. Porosity of 3D biomaterial scaffolds and osteogenesis. Biomaterials 2005;26(27):5474–91.
[7] Han Q, Wang C, Chen H, Zhao X, Wang JJABS. Engineering, Porous tantalum and titanium in orthopedics: a review 2019;5(11):5798–824.
[8] Long M, Rack HJ. Titanium alloys in total joint replacement–a materials science perspective. Biomaterials 1998;19(18):1621–39.
[9] Gao X, Fraulob M, Haiat G. Biomechanical behaviours of the bone-implant interface: a review. J R Soc Interface/the Royal Society 2019;16(156):20190259.
[10] Goodman SB. Wear particles, periprosthetic osteolysis and the immune system. Biomaterials 2007;28(34):5044–8.
[11] Sumner DR, Galante JO. Determinants of stress shielding: design versus materials versus interface. Clin Orthop Relat Res 1992;274:202–12.
[12] Huiskes R, Weinans H, van Rietbergen B. The relationship between stress shielding and bone resorption around total hip stems and the effects of flexible materials. Clin Orthop Relat Res 1992;274:124–34.
[13] Dick C, Georgii J, Burgkart R, Westermann R. Stress tensor field visualization for implant planning in orthopedics. Ieee T Vis Comput Gr 2009;15(6):1399–406.
[14] Murr LE, Gaytan SM, Martinez E, Medina F, Wicker RB. Next generation orthopaedic implants by additive manufacturing using electron beam melting. Int J Biomater 2012;2012:245727.
[15] Krishna BV, Bose S, Bandyopadhyay A. Low stiffness porous Ti structures for load-bearing implants. Acta Biomater 2007;3(6):997–1006.
[16] Bandyopadhyay A, Espana F, Balla VK, Bose S, Ohgami Y, Davies NM. Influence of porosity on mechanical properties and in vivo response of Ti6Al4V implants. Acta Biomater 2010;6(4):1640–8.
[17] Ciliveri S, Bandyopadhyay A. Influence of strut-size and cell-size variations on porous Ti6Al4V structures for load-bearing implants. J Mech Behav Biomed Mater 2022;126:105023.

[18] Fan S, Tan Z, Peng Z, Li S, Lei H, Qin Y, Fan H, Lin Y, Zhou C. Customized 3D printed porous titanium scaffolds with nanotubes loading antibacterial drugs for bone tissue engineering. Rev Adv Mater Sci 2024;63(1).
[19] Pei X, Wang L, Wu L, Lei H, Feng P, Fan C, Zhou Z, Wang L, Liu M, Zhou C, Kong Q, Fan Y. Heterogeneous porosity design triggered stress reorganization to avoid intervertebral cage subsidence and promote spinal fusion. Compos Struct 2023; 323:117516.
[20] Lei H, Zhou Z, Liu L, Gao C, Su Z, Tan Z, Feng P, Liu M, Zhou C, Fan Y, Zhang X. Icariin-loaded 3D-printed porous Ti6Al4V reconstruction rods for the treatment of necrotic femoral heads. Acta Biomater 2023;169:625–40.
[21] Chen C, Hao Y, Bai X, Ni J, Chung S-M, Liu F, Lee I-S. 3D printed porous Ti6Al4V cage: effects of additive angle on surface properties and biocompatibility; bone ingrowth in Beagle tibia model. Mater Des 2019;175.
[22] Ryu DJ, Jung A, Ban HY, Kwak TY, Shin EJ, Gweon B, Lim D, Wang JH. Enhanced osseointegration through direct energy deposition porous coating for cementless orthopedic implant fixation. Sci Rep 2021;11(1):22317.
[23] Huri PY, Ozilgen BA, Hutton DL, Grayson WL. Scaffold pore size modulates in vitro osteogenesis of human adipose-derived stem/stromal cells. Biomed Mater 2014;9 (4):045003.
[24] Ran Q, Yang W, Hu Y, Shen X, Yu Y, Xiang Y. Osteogenesis of 3D printed porous Ti6Al4V implants with different pore sizes. K.J.J.o.t.M.B.o.B.M. Cai 2018;84:1–11.
[25] Chen Z, Yan X, Yin S, Liu L, Liu X, Zhao G, Ma W, Qi W, Ren Z. E. C, Influence of the pore size and porosity of selective laser melted Ti6Al4V ELI porous scaffold on cell proliferation, osteogenesis and bone ingrowth. H.J.M.S. Liao 2020;106:110289.
[26] Luo C, Wang C, Wu X, Xie X, Wang C, Zhao C, Zou C, Lv F, Huang W, Liao J. Influence of porous tantalum scaffold pore size on osteogenesis and osteointegration: a comprehensive study based on 3D-printing technology. Mater Sci Eng C 2021;129:112382.
[27] Zhang Y, Sun N, Zhu M, Qiu Q, Zhao P, Zheng C, Bai Q, Zeng Q, Lu T. The contribution of pore size and porosity of 3D printed porous titanium scaffolds to osteogenesis. Biomater Adv 2022;133:112651.
[28] Wen CE, Yamada Y, Shimojima K, Chino Y, Asahina T, Mabuchi M. Processing and mechanical properties of autogenous titanium implant materials. J Mater Sci Mater Med 2002;13(4):397–401.
[29] Boccaccio A, Uva AE, Fiorentino M, Mori G, Monno G. Geometry design optimization of functionally graded scaffolds for bone tissue engineering: a mechanobiological approach. PLoS One 2016;11(1):e0146935.
[30] Han C, Li Y, Wang Q, Wen S, Wei Q, Yan C, Hao L, Liu J, Shi Y. Continuous functionally graded porous titanium scaffolds manufactured by selective laser melting for bone implants. J Mech Behav Biomed Mater 2018;80:119–27.
[31] Lee YKY, Jung AR, Heo SJ, Gweon B, Lim D. Influences of surface topography of porous titanium scaffolds manufactured by powder bed fusion on osteogenesis. J Mater Res Technol 2023;23:2784–97.
[32] Jain RK, Au P, Tam J, Duda DG, Fukumura D. Engineering vascularized tissue. Nat Biotechnol 2005;23(7):821–3.
[33] Rouwkema J, Rivron NC, van Blitterswijk CA. Vascularization in tissue engineering. Trends Biotechnol 2008;26(8):434–41.
[34] Mercado-Pagan AE, Stahl AM, Shanjani Y, Yang Y. Vascularization in bone tissue engineering constructs. Ann Biomed Eng 2015;43(3):718–29.
[35] Simunovic F, Finkenzeller G. Vascularization strategies in bone tissue engineering. Cells 2021;10(7).
[36] Artel A, Mehdizadeh H, Chiu YC, Brey EM, Cinar A. An agent-based model for the investigation of neovascularization within porous scaffolds. Tissue Eng 2011;17 (17–18):2133–41.
[37] Feng B, Jinkang Z, Zhen W, Jianxi L, Jiang C, Jian L, Guolin M, Xin D. The effect of pore size on tissue ingrowth and neovascularization in porous bioceramics of controlled architecture in vivo. Biomed Mater 2011;6(1):015007.
[38] Wang C, Xu D, Lin L, Li S, Hou W, He Y, Sheng L, Yi C, Zhang X, Li H, Li Y, Zhao W, Yu D. Large-pore-size Ti6Al4V scaffolds with different pore structures for vascularized bone regeneration. Mater Sci Eng C 2021;131:112499.
[39] Narayan D, Venkatraman SS. Effect of pore size and interpore distance on endothelial cell growth on polymers. J Biomed Mater Res 2008;87(3):710–8.
[40] Choi SW, Zhang Y, Macewan MR, Xia Y. Neovascularization in biodegradable inverse opal scaffolds with uniform and precisely controlled pore sizes. Adv Healthcare Mater 2013;2(1):145–54.
[41] Rezwan K, Chen QZ, Blaker JJ, Boccaccini AR. Biodegradable and bioactive porous polymer/inorganic composite scaffolds for bone tissue engineering. Biomaterials 2006;27(18):3413–31.
[42] Gerhardt LC, Boccaccini AR. Bioactive glass and glass-ceramic scaffolds for bone tissue engineering. Materials 2010;3(7):3867–910.
[43] Sudo H, Kodama HA, Amagai Y, Yamamoto S, Kasai S. In vitro differentiation and calcification in a new clonal osteogenic cell line derived from newborn mouse calvaria. J Cell Biol 1983;96(1):191–8.
[44] Tomlinson MJ, Dennis C, Yang XB, Kirkham J. Tissue non-specific alkaline phosphatase production by human dental pulp stromal cells is enhanced by high density cell culture. Cell Tissue Res 2015;361(2):529–40.
[45] Kocherova I, Bryja A, Mozdziak P, Angelova Volponi A, Dyszkiewicz-Konwinska M, Piotrowska-Kempisty H, Antosik P, Bukowska D, Bruska M, Izycki D, Zabel M, Nowicki M, Kempisty B. Human umbilical vein endothelial cells (HUVECs) Co-culture with osteogenic cells: from molecular communication to engineering prevascularised bone grafts. J Clin Med 2019;8(10).
[46] Mutschall H, Winkler S, Weisbach V, Arkudas A, Horch RE, Steiner D. Bone tissue engineering using adipose-derived stem cells and endothelial cells: effects of the cell ratio. J Cell Mol Med 2020;24(12):7034–43.
[47] Liu X, Zhao N, Liang H, Tan B, Huang F, Hu H, Chen Y, Wang G, Ling Z, Liu C, Miao Y, Wang Y, Zou X. Bone tissue engineering scaffolds with HUVECs/hBMSCs cocultured on 3D-printed composite bioactive ceramic scaffolds promoted osteogenesis/angiogenesis. Journal of Orthopaedic Translation 2022;37:152–62.
[48] Vestweber D. VE-cadherin: the major endothelial adhesion molecule controlling cellular junctions and blood vessel formation. Arterioscler Thromb Vasc Biol 2008; 28(2):223–32.
[49] Xie C, Gao Q, Wang P, Shao L, Yuan H, Fu J, Chen W, He Y. Structure-induced cell growth by 3D printing of heterogeneous scaffolds with ultrafine fibers. Mater Des 2019;181.
[50] Qin Y, Liu A, Guo H, Shen Y, Wen P, Lin H, Xia D, Voshage M, Tian Y, Zheng Y. Additive manufacturing of Zn-Mg alloy porous scaffolds with enhanced osseointegration: in vitro and in vivo studies. Acta Biomater 2022;145:403–15.
[51] Ren B, Wan Y, Liu C, Wang H, Yu M, Zhang X, Huang Y. Improved osseointegration of 3D printed Ti-6Al-4V implant with a hierarchical micro/nano surface topography: an in vitro and in vivo study. Mater Sci Eng C 2021;118:111505.